

# Morphology-Controlled Synthesis of ZnO Nanostructures by a Simple Round-to-Round Metal Vapor Deposition Route

Guozhen Shen,<sup>\*,†</sup> Yoshio Bando,<sup>‡</sup> Di Chen,<sup>‡</sup> Baodan Liu,<sup>‡</sup> Chunyi Zhi,<sup>†</sup> and Dmitri Golberg<sup>†</sup>

Advanced Materials Laboratory, National Institute for Materials Science (NIMS), Namiki 1-1, Tsukuba, Ibaraki 305-0044, Japan, and Division of Nano-Materials and Nano-Chemistry, Hefei National Laboratory for Physical Science at Microscale, University of Science and Technology of China, Hefei 230026, P. R. China

Received: November 23, 2005; In Final Form: January 15, 2006

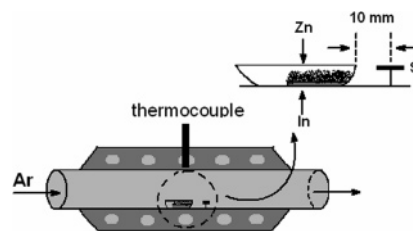
One-dimensional ZnO nanostructures with different morphologies have been successfully synthesized through a simple round-to-round metal vapor deposition route at 550 °C with a zinc powder covered indium film as the source material. The structures and morphologies of the products were characterized in detail by using X-ray diffraction, scanning electron microscopy, and transmission electron microscopy. Studies found that the morphology of the products can be easily tuned from one experimental round to another. Possible growth mechanisms for the formation of one-dimensional ZnO nanostructures with different morphologies are discussed. Photoluminescence studies show that there are sharp UV emission and broad defect-related green emissions for the products obtained in all experimental rounds. Relative intensity of the UV emission to defect-related emissions gradually increased from one experimental round to another.

## 1. Introduction

Zinc oxide, with a wide band gap of 3.37 eV and a large exciton binding energy of 60 meV at room temperature, is an important semiconducting and piezoelectric material. It is a smart material and has versatile applications in the fields of optoelectronics, piezoelectric sensors, transducers, and resonators. The wide band gap and large exciton binding energy make ZnO suitable for short wavelength optoelectronic applications and ensure an efficient excitonic emission at room temperature. ZnO is transparent to visible light and can be made highly conductive by doping. Element zinc is one of the most highly valuable elements for human beings. Its oxide, ZnO, is bio-safe and biocompatible and it can be directly used for biomedical applications without coating.<sup>1–3</sup> Since Yang<sup>3</sup> and co-workers reported on ZnO nanowire array nanolasers in 2001, synthesis and assembly of ZnO nanostructures, such as nanowires, nanobelts, and nanotubes, have been widely explored and many methods relying on vapor phase approaches and chemical solution process have been developed.<sup>1–20</sup> For example, well-aligned ZnO nanowire arrays were fabricated by using several different methods, such as template-assisted methods,<sup>4</sup> vapor transport and condensation methods,<sup>5,6</sup> metal–organic source vapor methods,<sup>7</sup> laser ablation methods,<sup>8</sup> and solution processes.<sup>9</sup> Some delicate hierarchical ZnO nanostructures with 2-, 4-, and 6-fold symmetries were obtained by the VTC process with use of ZnO, In<sub>2</sub>O<sub>3</sub>, and graphite powders at 950–1000 °C.<sup>10</sup> Wang<sup>11–13</sup> and co-workers have successfully fabricated a variety of ZnO nanostructures, such as nanorings, nanowire–nanoribbon junction arrays, mesoporous polyhedral cages and shells, nanopropellers, etc., by high-temperature VTC process using a ZnO powder as the source material.

Compared with the vapor phase processes of the ZnO nanostructure production with a ZnO powder as the source

## SCHEME 1: Experimental Setup Used for the Synthesis of ZnO Products



material, the metal vapor deposition (MVD) process is of particular importance from a technology point of view since much lower growth temperatures can be adopted.<sup>21,22</sup> In the typical MVD process, a metallic zinc powder was chosen as the zinc source. The Zn vapor pressure can reach up to 10.8 Pa at a temperature down to 400 °C, which makes the low-temperature MVD route much more facile and favorable than the high-temperature VTC methods. By using the MVD process, many kinds of complex ZnO nanoarchitectures have been synthesized,<sup>23,24</sup> including hollow ZnO urchins, microtrepangs of ZnO nanocones, microbelts of ZnO nanobowling-pin arrays, nanoflowers of ZnO nanobottles and nanonails, nanocombs, nanowheels of ZnO nanoarrows, nanofans, nanowire–nanobelt junctions, and microtubes by coalescence of ZnO nanowires and nanobarriers. These novel nanoarchitectures could be unique for many applications in nanotechnology.

In this work, we report on the controlled synthesis of one-dimensional ZnO nanostructures using a simple round-to-round MVD route at 550 °C in which a Zn powder covered In film was chosen as the source material.

## 2. Experimental Section

The one-dimensional ZnO nanostructures with different morphologies were fabricated by using a quartz tube furnace system, as shown in Scheme 1. First, the inner bottom of an alumina boat was deposited with a layer of thin indium film

\* To whom correspondence should be addressed. Fax: +81-29-851-6280. E-mail: shen.guozhen@nims.go.jp.

<sup>†</sup> National Institute for Materials Science.

<sup>‡</sup> University of Science and Technology of China.

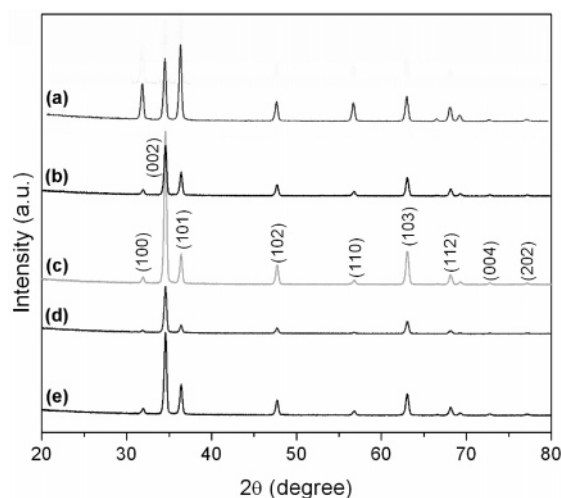


**Figure 1.** XRD patterns of the ZnO products obtained from the round-to-round metal vapor deposition process: (a) R1; (b) R2; (c) R3; (d) R4; and (e) R5.

(0.1 g). For the first round, the as-deposited indium film was covered with zinc powders (0.5 g, 100 mesh, 99.998%, Aldrich). Then the alumina boat was put in the hot zone of the tube and a piece of p-type silicon was placed next to the source materials and along the downstream side of the flowing gases. The vertical distance between the source materials and the substrate was about 10 mm. After the tube was purged with a high-purity Ar gas (99.999%) for 5 min, the furnace was heated to 550 °C and kept at this temperature for 60 min in flowing Ar gas (500 sccm) and O<sub>2</sub> gas (50 sccm). After cooling to room temperature, it was found that the whole substrate was covered with gray-white products. For the second round, the alumina boat was pulled out and the remaining powders in the boat were cleared. The silvery indium films still remained after one round. Another 0.5 g of zinc powders was put on the indium films and the boat was transferred to the furnace, and kept at the same conditions as those of Round 1. The experimental setup for Rounds 3–5 was similar to that of Round 2. In the experiments, it was found that the deposited indium film was consumed after five rounds.

The morphologies, structures, and compositions of the products were characterized by using X-ray diffraction (XRD, RINT 2200), scanning electron microscopy (SEM, JSM-6700), high-resolution transmission electron microscopy (HRTEM, JEM-3000F) equipped with an energy-dispersive X-ray spectrometer (EDS), and X-ray diffraction (XRD, Rigaku D/Max-2500). Photoluminescence (PL) was studied at room temperature with use of a continuous-wave He–Cd laser with 325 nm line.

### 3. Results and Discussion

The round-to-round MVD process was performed in a horizontal tube furnace system. The source materials were ZnO powder covered indium films. In the experiments, it was found that the deposited indium films were depleted after five rounds. For all the rounds, after reaction, it was found that the whole silicon substrate was covered with gray-white product. Figure 1 shows the typical X-ray diffraction (XRD) patterns of the product obtained from the first round to the fifth round. The peaks in all these patterns can be readily indexed to pure wurtzite ZnO with cell dimensions comparable to the reported values (Joint Committee on Powder Diffraction Standards, JCPDS Card No. 36-1451). No peaks of other impurities such as Zn, In<sub>2</sub>O<sub>3</sub>, etc. were detected, indicating the formation of a pure ZnO product. In Figure 1b–e, the (002) peak is the dominant peak,

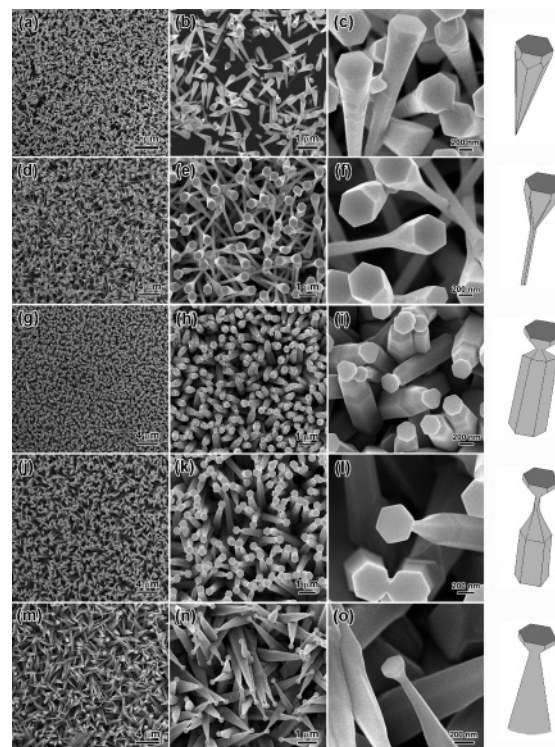


**Figure 2.** SEM images of deposited ZnO products after the MVP process: (a–c) R1; (d–f) R2; (g–i) R3; (j–l) R4; and (m–o) R5. The right-hand-side parts of each row are the corresponding structural models.

and its intensity is much higher than other peaks, presumably revealing the preferable (001) growth orientation of the ZnO products.

The product morphology was examined by scanning electron microscopy (SEM), as shown in Figure 2. For the product obtained in the first round (R1), SEM images show that the obtained ZnO structures in R1 are of cone-like morphology. In other words, ZnO nanocones are deposited on the whole substrate. The high-magnification SEM image (Figure 2c) indicates that each ZnO nanocone has a diameter gradually increasing from about 50 nm at the root to 300 nm at the tip-ends possessing perfect atomically flat hexagonal-shaped morphology. By contrast, for the ZnO products obtained in the second round (R2), SEM images (Figure 2d–f) show that they are ZnO nanonails with large caps. The lengths of the ZnO nanonails are about 4 μm and each ZnO nanonail has a stem with a diameter of about 100 nm with a large diameter hexagonal-shaped cap attached. The length of the side of the large diameter hexagonal-shaped cap is about 300 nm according to the SEM observations. Panels g–i in Figure 2 are the SEM images of the ZnO products obtained in the third round (R3). They show that the products are still of nanonail morphology. However, compared with the ZnO nanonails obtained in R2, each ZnO nanonail in R3 consists of a hexagonal prism stem and a hexagonal-shaped cap connected to a small diameter neck. The diameter of the stem is about 300 nm, much larger than that of the ZnO nanonail in R2. For the products obtained in the fourth round (R4), SEM images (Figure 2j–l) show that they are also composed of hexagonal prism stems and hexagonal-shaped caps connected to small diameter necks as those in R3 except that the lengths of the necks are much longer, 300–400 nm. Panels m–o of Figure 2 are the SEM images of the ZnO products obtained in the fifth round (R5). They clearly show the formation of nanonails composed of cone-like stems connected with hexagonal-shaped caps. The diameters of the



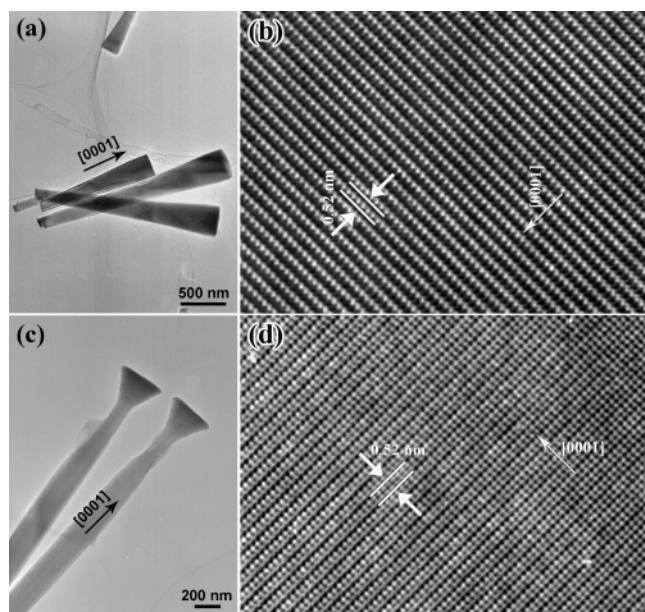


**Figure 3.** (a) TEM image and (b) HRTEM image of the ZnO nanocones obtained in Round 1. (c) TEM image and (d) HRTEM image of the ZnO nanonails obtained in Round 4.

stems gradually decrease from about 500 nm at the base to 50 nm at the top and the hexagonal-shaped caps have diameters of about 200 nm, similar with those obtained in R3. In the present work, it was found that the indium was depleted after five experimental rounds and only ZnO nanoprisms are obtained after that (see the following discussions).

The microstructures of the products obtained in different rounds were also checked with high-resolution transmission electron microscopy (HRTEM). Figure 3a is the TEM image of the ZnO nanocones obtained in R1. The length of each ZnO nanocone is several hundred nanometers to several micrometers. The diameter of a ZnO nanocone ranges from 50 nm in the bottom to about 300 nm in the top, in accordance with the SEM results. The corresponding atomically resolved HRTEM image is shown in Figure 3b. The measured plane spacing is about 0.52 nm, corresponding to the (0001) plane of ZnO. The image also shows that the surface of the ZnO nanonail is relatively clean and no amorphous layer is observed. No dislocations or stacking faults are observed in the areas examined. Figure 3c depicts the TEM image of the ZnO nanonails obtained in R4. It shows the formation of the ZnO nanonail composed of a stem and a cap connected with a small diameter neck. The lattice fringes within the ZnO nanonail are separated by  $\sim 0.52$  nm, corresponding to the (0001) fringes perpendicular to the growth direction, which is consistent with that of the bulk wurtzite ZnO crystal. TEM analysis of the products obtained in other rounds gives similar results. It indicates that all the ZnO products have the same (0001) growth direction though they have quite different morphologies.

During the experiments, it was found that at the edge of the silicon substrate near the source material novel comblike ZnO nanostructures are formed for all the experimental rounds (from R1 to R5). The SEM images of the ZnO nanocombs are shown in Figure 4a–i. The images show that all the ZnO nanocombs are composed of one-dimensional ZnO nanostructure arrays grown perpendicularly on one side of a nanobelt stem. The morphology of the one-dimensional ZnO nanostructure arrays is in accordance with those discussed in Figure 2. The formation of ZnO nanocombs at the site near the source material is in

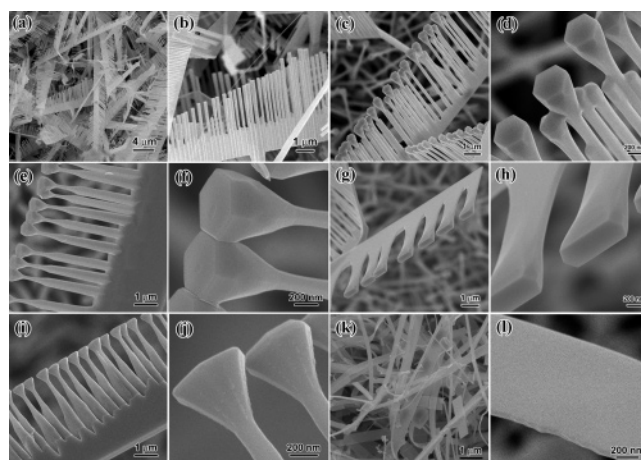


**Figure 4.** SEM images with different magnifications of a ZnO product deposited on the alumina boat near the source materials from (a, b) R1, (c, d) R2, (e, f) R3, (g, h) R4, and (i, j) R5. (k, l) SEM images of the ZnO nanobelts obtained after the MVP process.

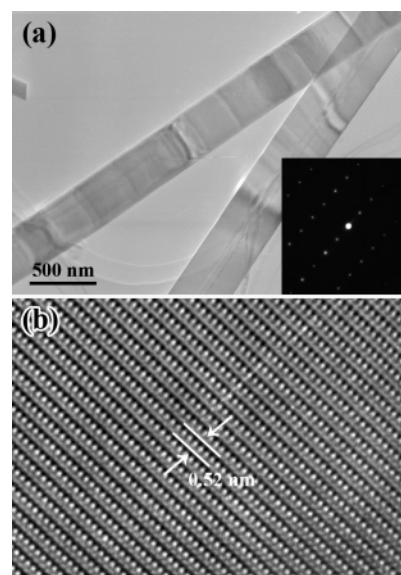


**Figure 5.** (a) TEM and (b) HRTEM images of the ZnO nanobelts obtained during the MVP process. The inset in part a is the corresponding SAED pattern.

agreement with the previous reports that ZnO nanocombs favor to deposit on the site where the gas concentrations are high.

In the experiments, it was also found that ZnO nanobelts could be obtained on the surface of an alumina boat near the source material and the SEM images are shown in Figure 4k,l. Each ZnO nanobelt has a width of several hundred nanometers and a length up to several hundred micrometers. The thickness of the ZnO nanobelt is quite thin,  $\sim 50$  nm. Figure 5a is the TEM image of two ZnO nanobelts with widths of 300 and 400 nm, respectively. The inset selected area electron diffraction (SAED) pattern was taken from a ZnO nanobelt with an electron beam along its [100] zone axis. It, together with the HRTEM image shown in Figure 5b, confirms that the ZnO nanobelt grows along the [0001] direction.

We have found that indium was depleted after five experimental rounds and only ZnO nanoprisms are obtained after that. The product obtained in the sixth round is of the same morphology as those obtained when only zinc powder is used as the evaporated source material. Panels a–c of Figure 6 are the SEM images of a product when only zinc powder is thermally evaporated in the reaction system. The whole silicon

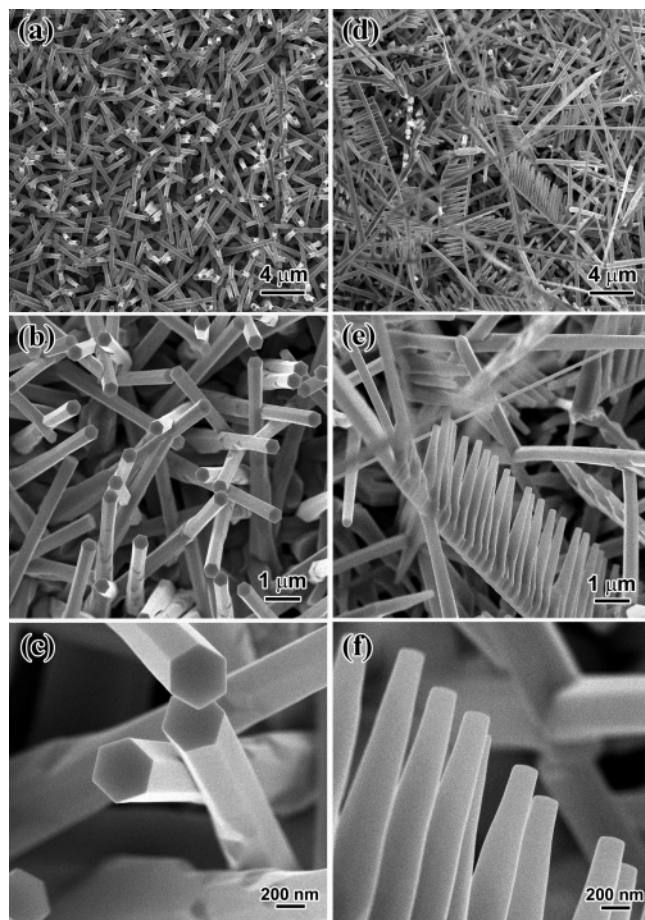


**Figure 6.** (a–c) SEM images of ZnO nanoprisms synthesized during the MVP process when only zinc powder was chosen as the source material. (d–f) SEM images of ZnO nanocombs synthesized during the MVP process when only a mixture of zinc powder and indium powder was used as the source material.

substrate was covered with prism-like products, as indicated in this figure. The ZnO nanoprisms are of well-faceted hexagonal shapes and about 200 nm in diameter and several micrometers in length. The high-magnification SEM image in Figure 6c clearly displays the hexagonal shape of the ZnO nanoprisms. The surfaces of these nanoprisms are quite smooth without any nanoparticle impurities. During the experiments, it was also found that if an indium film was replaced by indium powders, while all other experimental parameters were kept constant, only nanocombs formed through the alignment of ZnO nanocone arrays on either side of ZnO nanowires, as shown in Figure 6d–f.

Characterization by SEM, XRD, EDX, and TEM verified that no metallic particles were observed at the tips of the synthesized ZnO nanostructures. This indicates that the synthesized ZnO nanostructures were self-assembled through a vapor–solid (VS) mechanism, instead of the vapor–liquid–solid (VLS) mechanism. Due to the intrinsic properties, it is easy for wurtzite ZnO to grow into anisotropic one-dimensional nanostructures. Though the VS mechanism is the dominant mechanism to explain the growth of anisotropic one-dimensional nanostructures, it cannot be used to explain the morphology variations of the synthesized ZnO nanostructures in the round-to-round MVD process. Though various nanostructures with similar morphologies have been reported for carbon and carbon nitride,<sup>25</sup> it was thought that the formation of present nanostructures has a quite different growth mechanism compared with those of carbon-related nanostructures since they have quite different intrinsic crystal

structures. The formation of the present complex nanostructures indicates that complicated reactions may occur during the present experiments. It was thought that the present ZnO nanostructures with big caps are nucleated by ZnO solid, or zinc suboxide, or liquid zinc metal droplets generated during the thermal evaporation process at high temperature. After saturation, small ZnO nanorods will sprout out epitaxially from the silicon substrate. The incoming ZnO<sub>x</sub> vapor then deposits epitaxially on both the shaft and cap of the small nanorod sprout. It is well-known that the caps have better chances to adsorb the ZnO<sub>x</sub> vapor than the bottoms, and the amount of ZnO<sub>x</sub> vapor adsorbed increases with the increase of the diameter of hexagonal cap. That is why usually the cap is much bigger than the shaft. The ZnO<sub>x</sub> vapor adsorbed on the bottom will push up the nanorod and increase its length. These processes are in agreement with previous reports on ZnO nanostructures with bigger diameter caps.<sup>10</sup>

Besides the above discussions, in the present round-to-round MVD process, all the experiments were performed under the same experimental conditions except for different contents of indium, since indium was gradually consumed from round to round. We found that it is highly reproducible to obtain the ZnO nanostructures in our reaction system. So, in the present round-to-round MVD process the formation of one-dimensional ZnO nanostructures with different morphologies is mainly governed by the indium content in the reaction system. It is well-known that in the In–Zn–O system the homologous compounds In<sub>2</sub>O<sub>3</sub>(ZnO)<sub>*n*</sub> (*n* = integer) may form. It is thought that the morphology variations noticed in the present work are also due to the formation of In<sub>2</sub>O<sub>3</sub>(ZnO)<sub>*n*</sub> compounds with different *n* numbers, though we did not detect the existence of indium in EDX spectra. This may be due to the extremely low concentration of indium in the ZnO nanostructures (the detection limit of EDS for indium is ~5 atom %). The homologous compounds In<sub>2</sub>O<sub>3</sub>(ZnO)<sub>*n*</sub> (*n* = integer) were first found by Cannard and Tilley<sup>26a</sup> and Kasper.<sup>26b</sup> They reported that a homologous compound is a layered structure. Our group has also proposed the structure model where the structure is built up of a succession of InO<sub>2</sub><sup>1–</sup> (In–O layer) and MZn<sub>*n*</sub>O<sub>*n*+1</sub><sup>1–</sup> (M/Zn–O layer) layers along the *c* axis.<sup>27</sup> Figure 7 shows the typical structure models for the InMO<sub>3</sub>(ZnO)<sub>*n*</sub> (M = In) projected along the [100] directions. In the structures, oxygen atoms are arranged in a hexagonal packing along the *c*<sub>m</sub>\*(*c*<sub>0</sub>\*) axis, in which they are stacked as ABAB within a M/Zn–O layer and changed into CACA across an In–O layer. The M and Zn atoms occupy either tetragonal or trigonal bipyramidal positions, whereas the In atoms occupy the octahedral positions. In the present experiments, the concentration of indium gradually decreases from one round to another. Thus In<sub>2</sub>O<sub>3</sub>(ZnO)<sub>*n*</sub> compounds with different *m* numbers may form during the experiments and different *m* values result in different M/Zn–O layer numbers between two In–O layers. This, in turn, leads to the prominent structural variation and thus various one-dimensional ZnO nanostructures form. With the increase of *n*, indium content in the InMO<sub>3</sub>(ZnO)<sub>*n*</sub> compound will decrease, which can explain why we did not observe the existence of indium using EDX (if the content of indium decreased to below 5%).

It is generally believed that the morphology of ZnO nanostructures is mainly influenced by the growth temperature and gas-phase supersaturation, etc.<sup>28</sup> In the present work, all the experiments were performed in the same reaction system and the heating rate of the furnace and the gas flow rate were well controlled by the same controller. So it was thought that, besides



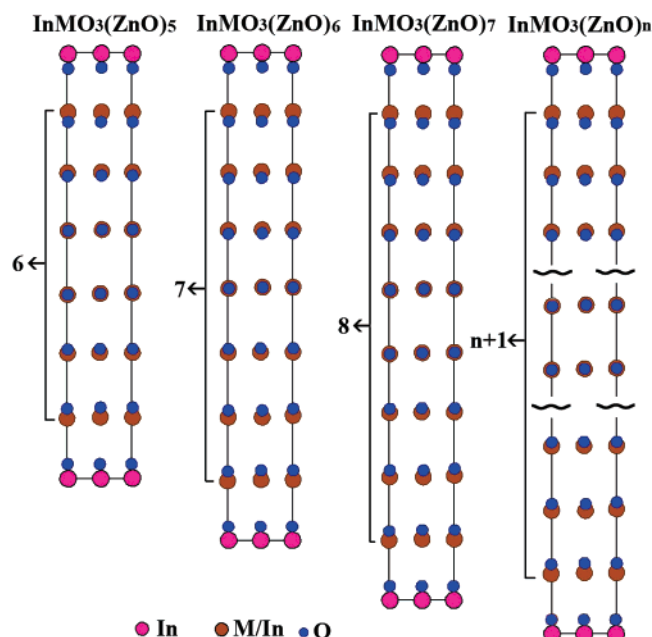


**Figure 7.** Structure models for the  $\text{InMO}_3(\text{ZnO})_n$  ( $M = \text{In}$ ) homologous compounds projected along the  $[100]$  directions: (a)  $n = 5$ , (b)  $n = 6$ , and (c)  $n = 7$ .

the effect of formation of  $\text{In}_2\text{O}_3(\text{ZnO})_m$  compounds with different  $m$  numbers on the morphologies of the final products, the formation of the present different ZnO nanostructures was also influenced by the gas concentrations in the reaction system. With the increase of experimental rounds, indium will be gradually consumed, which resulted in the change of indium gas concentrations in the reaction system. The change of indium gas concentrations will then affect the zinc gas concentrations, thus ZnO nanostructures with different morphologies will be formed from different experimental rounds.

Finally, we measured the room temperature photoluminescence (PL) properties of the as-grown one-dimensional ZnO nanostructures. According to literature, ZnO usually exhibits two strong emission peaks, near-band-edge and green broadband, respectively. The near-band-edge emission peak is attributed to the direct recombination of excitons through an exciton–exciton collision process. In fact, the green broadband is a mixture of the blue, green, and yellow emissions. Compared with the near-band-edge emission, the explanations on the origins of the green emissions are still preliminary. For example, it was explained that the green emission suggested optical transitions in the single ionized oxygen vacancy ( $\text{V}_\text{O}^+$ ), and the yellow emission implied optical transitions in the single negatively charged interstitial oxygen ion ( $\text{O}_\text{i}^-$ ) inside the ZnO crystal structure.<sup>29a</sup> Other green band transition mechanisms were also suggested, such as donor–acceptor<sup>29b</sup> and shallow donor–deep level transitions,<sup>29c</sup> zinc interstitials, and antisite oxygen.<sup>30</sup> Figure 8 depicts the PL spectra of the one-dimensional ZnO nanostructures synthesized in the round-to-round MVD process. For comparison, the PL spectra of the ZnO nanoprisms (S1) synthesized from a pure zinc powder are also shown in this figure. It is clear that all the spectra of one-dimensional ZnO nanostructures obtained from different experimental rounds, as well as the ZnO nanoprisms from pure zinc powder, exhibit a sharp UV emission at around 380 nm and broad green emissions ranging from 450 to 750 nm. Careful analysis shows that the broad green emissions ranging from 450 to 750 nm consist of three emissions centered at 495, 602, and 647 nm. According to the literature, the UV emission of the ZnO

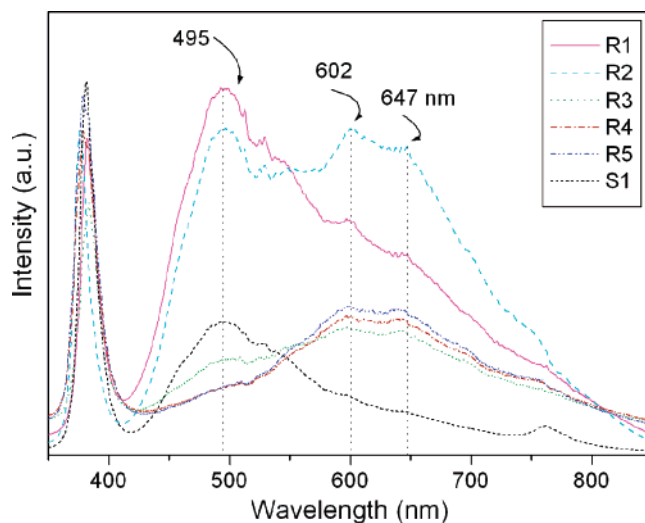


**Figure 8.** Room temperature PL spectra of the ZnO products obtained during the round-to-round MVP process.

**TABLE 1: The Relative Intensity of UV Emission to Green Emission for the ZnO Products Obtained in Different Rounds**

| sample no. | rel intensity (UV emission/<br>green emission) |
|------------|--|
| R1         | 0.86   |
| R2         | 1.0  |
| R3         | 1.98   |
| R4         | 2.34   |
| R5         | 2.40   |
| S1         | 2.82   |

nanostructures synthesized in the round-to-round MVD process, Figure 8, with a peak at  $\sim 380$  nm corresponds to the near-band-edge (NBE) transition. The latter is responsible for the recombination of free excitons in ZnO. The exact origins of the green emissions are still unclear. However, it should be stressed that they are obviously defects—related to emissions according to the previous reports. From the PL spectra, it was found that the relative intensity of the three emissions among the green emissions centered at 495, 602, and 647 nm are different for different products. For the product obtained in R1, the peak at 495 nm is the strongest peak and it is much stronger than the other two peaks, while for other products obtained in R2, the peaks at 495, 602, and 647 nm have almost the same peak intensity. For the product obtained in R3–R5, the intensity of the peak at 495 nm is much weaker than the other two peaks at 602 and 647 nm, which have similar peak intensities, as shown in Figure 8. Besides the difference in the relative peak intensity in the green emissions, the relative intensity of the NBE band to the green emission band also changes with the experimental round number. From the PL spectra, the relative intensity of NBE to green emission is 0.86 for R1, 1.0 for R2, 1.98 for R3, 2.34 for R4, and 2.40 for R5. For the ZnO nanoprisms (S1) synthesized from pure zinc powder it shows the strongest relative intensity of 2.82 (Table 1). This indicates that with a decrease of the indium concentration, the product photoluminescence properties are improved.

#### 4. Conclusion

One-dimensional ZnO nanostructures with different morphologies have been successfully synthesized by using a simple round-to-round metal vapor deposition process. The formation of  $\text{In}_2\text{O}_3(\text{ZnO})_m$  compounds with different  $m$  values was deduced to explain their growth process, since all the experiments were

performed under the same experimental conditions, except for different indium contents in each consecutive experimental round. Photoluminescence studies show that there are sharp UV emission and broad defect-related green emissions for the products obtained in all experimental rounds. The relative intensity of the UV emission to defect-related emissions gradually increased from one experimental round to another.

**Acknowledgment.** We thank Y. Uemura for advice during material synthesis and K. Kurashima for technical assistance in TEM work.

## References and Notes

- (1) Pan, Z. W.; Dai, Z. R.; Wang, Z. L. *Science* **2001**, *291*, 1947.
- (2) Wang, Z. L.; Kong, X. Y.; Ding, Y.; Gao, P. X.; Hughes, W. L.; Yang, R. S.; Zhang, Y. *Adv. Funct. Mater.* **2004**, *14*, 943.
- (3) Huang, M. H.; Mao, S.; Feick, H.; Yan, H. Q.; Wu, Y. Y.; Kind, H.; Weber, E.; Russo, R.; Yang, P. D. *Science* **2001**, *292*, 1897.
- (4) (a) Fan, H. J.; Lee, W.; Scholz, R.; Dadgar, A.; Krost, A.; Nielsch, K.; Zacharias, M. *Nanotechnology* **2005**, *16*, 913. (b) Li, Y.; Meng, G. W.; Zhang, L. D.; Philipp, F. *Appl. Phys. Lett.* **2000**, *76*, 2011.
- (5) (a) Huang, M. H.; Wu, Y.; Feick, H.; Tran, N.; Weber, E.; Yang, P. D. *Adv. Mater.* **2001**, *13*, 113. (b) Cheng, H. M.; Hsu, H. C.; Tseng, Y. K.; Lin, L. J.; Hsieh, W. F. *J. Phys. Chem. B* **2005**, *109*, 8749. (c) Jie, J. S.; Wang, G. Z.; Wang, Q. T.; Chen, Y. M.; Han, X.; Wang, X.; Hou, J. G. *J. Phys. Chem. B* **2004**, *108*, 11976.
- (6) (a) Tseng, Y. K.; Huang, C. J.; Cheng, H. M.; Lin, I. N.; Liu, K. S.; Cheng, I. C. *Adv. Funct. Mater.* **2003**, *13*, 811. (b) Geng, C. Y.; Jiang, Y.; Yao, Y.; Meng, X. M.; Zapien, J. A.; Lee, C. S.; Lifshitz, Y.; Lee, S. T. *Adv. Funct. Mater.* **2004**, *14*, 589. (c) Wang, X. D.; Song, J. H.; Li, P.; Ryou, J. H.; Dupuis, R. D.; Summers, C. J.; Wang, Z. L. *J. Am. Chem. Soc.* **2005**, *127*, 7920.
- (7) (a) Park, W. I.; Kim, D. H.; Jung, S. W.; Yi, G. C. *Appl. Phys. Lett.* **2002**, *80*, 4232. (b) Wu, J. J.; Liu, S. C. *Adv. Mater.* **2002**, *14*, 215.
- (8) Sun, Y.; Fuge, G. M.; Ashfold, M. N. R. *Chem. Phys. Lett.* **2004**, *396*, 21.
- (9) (a) Vayssieres, L. *Adv. Mater.* **2003**, *15*, 464. (b) Li, Q. C.; Kumar, V.; Li, Y.; Zhang, H. T.; Chang, R. P. H. *Chem. Mater.* **2005**, *17*, 1001.
- (10) (a) Lao, J. Y.; Huang, J. Y.; Wang, D. Z.; Ren, Z. F. *Nano Lett.* **2003**, *3*, 235. (b) Lao, J. Y.; Wen, J. G.; Ren, Z. F. *Nano Lett.* **2002**, *2*, 1287.
- (11) (a) Kong, X. Y.; Ding, Y.; Yang, R.; Wang, Z. L. *Science* **2004**, *303*, 1348. (b) Gao, P. X.; Ding, Y.; Mai, W. J.; Hughes, W. L.; Lao, C. S.; Wang, Z. L. *Science* **2005**, *309*, 1700.
- (12) (a) Gao, P. X.; Wang, Z. L. *Appl. Phys. Lett.* **2004**, *84*, 2883. (b) Wang, Z. L.; Kong, X. Y.; Zuo, J. M. *Phys. Rev. Lett.* **2003**, *91*, 185502.
- (13) (a) Gao, P. X.; Wang, Z. L. *J. Am. Chem. Soc.* **2003**, *125*, 11299. (b) Gao, P. X.; Wang, Z. L. *J. Phys. Chem. B* **2002**, *106*, 12653.
- (14) (a) Kong, Y. C.; Yu, D. P.; Zhang, B.; Fang, W.; Feng, S. Q. *Appl. Phys. Lett.* **2001**, *78*, 407. (b) Wu, J. J.; Liu, S. C. *Adv. Mater.* **2003**, *15*, 464.
- (15) (a) Yao, B. D.; Chan, Y. F.; Wang, N. *Appl. Phys. Lett.* **2002**, *81*, 757. (b) Park, W. I.; Yi, G. C.; Kim, M. Y.; Pennycook, S. J. *Adv. Mater.* **2002**, *14*, 1841.
- (16) (a) Hu, J. Q.; Bando, Y. *Appl. Phys. Lett.* **2003**, *82*, 1401. (b) Hu, J. Q.; Bando, Y.; Zhan, J. H.; Li, Y. B.; Sekiguchi, T. *Appl. Phys. Lett.* **2003**, *83*, 4414.
- (17) (a) Wan, Q.; Li, Q. H.; Chen, Y. J.; Wang, T. H.; He, X. L.; Li, J. P.; Lin, C. L. *Appl. Phys. Lett.* **2004**, *84*, 3654. (b) Ng, H. T.; Li, J.; Smith, M. K.; Nguyen, P.; Cassell, A.; Han, J.; Meyyappan, M. *Science* **2003**, *300*, 1249.
- (18) (a) Liu, B.; Zeng, H. C. *J. Am. Chem. Soc.* **2003**, *125*, 4430. (b) Liu, B.; Zeng, H. C. *J. Am. Chem. Soc.* **2004**, *126*, 8124. (c) Zhang, J.; Sun, L. D.; Liao, C.; Yan, C. H. *Chem. Commun.* **2002**, 262.
- (19) (a) Chang, P. C.; Fan, Z. Y.; Wang, D. W.; Tseng, W. Y.; Chiou, W. A.; Hong, J.; Lu, J. G. *Chem. Mater.* **2004**, *16*, 5133. (b) Hu, P.; Liu, Y.; Wang, X.; Fu, L.; Zhu, D. B. *Chem. Commun.* **2003**, 1304.
- (20) (a) Liu, C. H.; Zapien, J. A.; Yao, Y.; Meng, X. M.; Lee, C. S.; Fan, S. S.; Lifshitz, Y.; Lee, S. T. *Adv. Mater.* **2003**, *15*, 838. (b) Zhang, B. P.; Binh, N. T.; Segawa, Y.; Wakatsuki, K.; Usami, N. *Appl. Phys. Lett.* **2003**, *83*, 1635.
- (21) (a) Zhang, X.; Zhang, Y.; Xu, J.; Wang, Z.; Chen, X.; Yu, D. P.; Zhang, P.; Qi, H.; Tian, Y. *Appl. Phys. Lett.* **2005**, *87*, 123111. (b) Wang, R. C.; Liu, C. P.; Huang, J. L.; Chen, S. J.; Tseng, Y. K.; Kung, S. C. *Appl. Phys. Lett.* **2005**, *87*, 013110.
- (22) (a) Wang, R. C.; Liu, C. P.; Huang, J. L.; Chen, S. J. *Appl. Phys. Lett.* **2005**, *86*, 251104. (b) Liao, L.; Li, J. C.; Liu, D. H.; Liu, C.; Wang, D. F.; Song, W. Z.; Fu, Q. *Appl. Phys. Lett.* **2005**, *86*, 083106.
- (23) (a) Shen, G. Z.; Bando, Y.; Lee, C. J. *J. Phys. Chem. B* **2005**, *109*, 10578. (b) Shen, G. Z.; Bando, Y.; Lee, C. J. *J. Phys. Chem. B* **2005**, *109*, 10779.
- (24) (a) Shen, G. Z.; Cho, J. H.; Lee, C. J. *Chem. Phys. Lett.* **2005**, *401*, 414. (b) Shen, G. Z.; Bando, Y.; Liu, B. D.; Golberg, D.; Lee, C. J. *Adv. Funct. Mater.* **2006**, *16*, 410. (c) Jeong, J. S.; Lee, J. Y.; Cho, J. H.; Suh, H. J.; Lee, C. J. *Chem. Mater.* **2005**, *17*, 2752.
- (25) (a) Zhang, G. Y.; Jiang, X.; Wang, E. G. *Science* **2003**, *300*, 472. (b) Wang, E. G. *Adv. Mater.* **1999**, *11*, 1129. (c) Wang, E. G. *Prog. Mater. Sci.* **1997**, *41*, 241.
- (26) (a) Cannard, P. J.; Tilley, R. J. D. *J. Solid State Chem.* **1998**, *73*, 418. (b) Kasper, H. Z. *Anorg. Allg. Chem.* **1967**, *349*, 113.
- (27) (a) Li, C. F.; Bando, Y.; Nakamura, M.; Onoda, M.; Kimizuka, N. *J. Solid State Chem.* **1998**, *139*, 347. (b) Li, C. F.; Bando, Y.; Nakamura, M.; Kurashima, K.; Kimizuka, N. *Acta Crystallogr. Sect. B* **1999**, *55*, 355.
- (28) (a) Ye, C. H.; Fang, X. S.; Hao, Y. F.; Teng, X. M.; Zhang, L. D. *J. Phys. Chem. B* **2005**, *109*, 19758. (b) Leung, Y. H.; Djuricic, A. B.; Gao, J.; Xie, M. H.; Chan, W. K. *Chem. Phys. Lett.* **2004**, *385*, 155.
- (29) (a) Wu, X. L.; Siu, G. G.; Fu, C. L.; Ong, H. C. *Appl. Phys. Lett.* **2001**, *78*, 2285. (b) Reynolds, D. C.; Look, D. C.; Jogai, B. *J. Appl. Phys.* **2001**, *89*, 6189. (c) Liu, M.; Kitai, A. H.; Mascher, P. *J. Lumin.* **1992**, *54*, 35.
- (30) (a) Liu, B.; Fu, Z.; Jia, Y. *Appl. Phys. Lett.* **2001**, *79*, 943. (b) Hu, J. Q.; Ma, X. L.; Xie, Z. Y.; Wong, N. B.; Lee, C. S.; Lee, S. T. *Chem. Phys. Lett.* **2001**, *344*, 97. (c) Lyu, S. C.; Zhang, Y.; Lee, C. J.; Ruh, H.; Lee, H. J. *Chem. Mater.* **2003**, *15*, 3294.